Newcastle University Eprint version
This article has been accepted for publication in a future issue of this journal, but has not been fully edited. Content may change prior to final publication. Citation information: DOI 10.1109/TIA.2019.2918499
IEEE Transactions on Industry Applications 2019

Design and Analysis of a Flux Concentrated Linear Vernier Hybrid Machine with Consequent Poles

A A. Almoraya, Student Member, IEEE, N. J. Baker, K.J. Smith, M.A.H. Raihan

***Abstract* -- In low speed applications, variable reluctance permanent magnet machines are often proposed due to their efficient use of magnet material and high torque density. This becomes even more important in large linear applications, where the translator is longer than the stator. Often, however, very low power factors are experienced by this class of machine. This paper proposes a V-shape flux concentrated version of a consequent pole linear Vernier hybrid permanent magnet machine and compares it to a surface mounted magnet variant. Using finite element analysis validated by two laboratory prototypes, it is shown that the flux concentrated version increases the airgap flux density, which potentially leads to an improvement in the force density and efficiency, or can be used to increase the operating power factor.**

***Index Terms*-- consequent pole, V-shape, Vernier machine, power factor, linear machine, leakage flux.**

I. Introduction

In low speed direct drive applications, permanent magnet (PM) machines with a small pole width can be used to increase the rate of change of flux linkage. For conventional linear permanent magnet machines, small magnet poles would result in a large number of slots, with a corresponding increase in the overall size of the machine and the associated costs as discussed in [1]. Vernier permanent magnet (VPM) Machines have been developed for low-speed high torque direct-drive applications, either in rotary [2-5] or linear versions [6, 7]. Multiple magnets are mounted on each stator tooth and hence the flux from several magnets links a single coil. The interaction of small magnets and rotor teeth gives a magnetic gearing effect and allows a small number of stator slots to encompass a large number of magnet poles. An unfortunate downside of this is that the coil driven flux sees a low reluctance, giving characteristically high inductance and a naturally low operating power factor [8-10]. In the last two decades a lot of research has been carried out on the VPM machines in order to improve their electromagnetic and electrical performances including torque density, efficiency and power factor [8, 9, 11, 12]. Since both PMs and windings are placed on the stator, the linear version is attractive in long stroke applications.

The conventional VPM machine has adjacent magnets spanning a full pole directly in contact with each other – a surface mounted PM configuration. A salient translator then switches the direction of flux cutting the stator coils. As adjacent magnets must have reversed polarity, only half of the magnets produce the main flux, while the remainder, which are aligned with a translator slot, produce mainly leakage flux [13, 14]. As the cost of manufacturing of the VPM machine is likely to be driven by the amount of PM material, it has been proposed to use a consequent pole topology [14-16] where alternate magnets are replaced with soft magnetic poles (teeth). The stator of this configuration now consists of inset rectangular magnets magnetized in a common direction and separated by soft magnetic poles, Fig. 1(a). Whilst magnet saving can be realised, these consequent pole machines still suffer from low power factor as overall reluctance is similar to the surface mounted version.

One method of improving power factor is to increase magnetic loading, and reduce electric loading. Magnetic loading can be increased by using flux concentration, for example by splitting pole magnets into a V–shape [17]. Therefore in a flux concentrated consequent pole VPM machine configuration, each magnet pole comprises of two magnets forming a V-shape, Fig. 1(b). This topology, initially reported in [18], hence possesses a combination of consequent poles, flux concentration and flux switching machine topologies. The use of V-shaped PM arrays without consequent poles has been proposed for rotary VPM [19, 20]

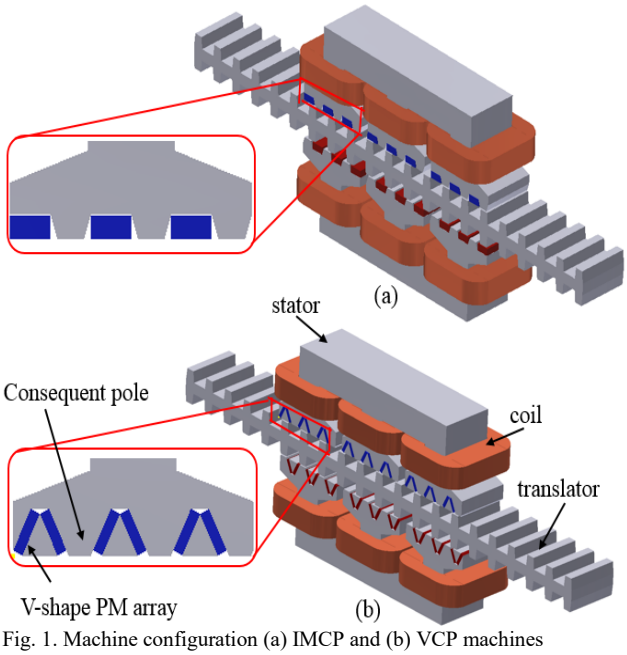

Fig. 1. Machine configuration (a) IMCP and (b) VCP machines

This work was supported in part by the UK EPSRC under Grant EP/N021452/1. A. A. Almoraya and all authors are with the School of Engineering, Newcastle University, Newcastle Upon Tyne, NE1 7RU, U.K. (e-mail: a.a.a.almoraya@ncl.ac.uk)

machines, and linear VPM machines [21]. The key feature of the V-shape machine discussed here compared to that found in existing literature is the flux concentration effect resulting from the replacement of the inset rectangular PMs with V-shape PMs in a consequent pole machine.

The main purpose of this paper is to compare the Inset Magnet Consequent Pole (IMCP) and proposed V-shape Consequent Pole (VCP) topologies when both machines have the same overall volume and PM mass. It is shown that the proposed VCP topology can reduce the leakage flux and improve the airgap flux density from PMs, improving force capability and operating power factor for a fixed MMF. This in turn can lead to a lower electric loading for a given force and hence a further improved power factor.

II. Machine Configuration and Operation Principle

A. Configuration

Fig. 1(a) shows the structure of the IMCP machine, including two stator cores where both the PMs and armature windings are mounted. Each stator side has three teeth which are displaced by 120 electrical degrees in order to obtain a three-phase machine. Fig 1(b) shows the flux concentrated version, where a combination of V-shape PM arrays and consequent poles are utilized. Magnet flux is channelled by a triangular pole piece, which is glued in place without the need for iron ribs, as has been proposed in rotary machines [17] . Removal of the ribs increases the reluctance of the four leakage flux paths around the magnet edges. The translator, which sits between both stator sides, is constructed as a simple laminated iron core with salient teeth offering a rigid structure to deliver high thrust force.

B. Operation Principle

Fig. 2 demonstrates the operation principle of the VCP machine by way of idealized magnet driven flux flow at four key positions. The IMCP machine operates in an identical manner. Fig. 2 (a) shows the translator teeth aligned with the phase B magnet poles of the upper stator, corresponding to peak magnet flux linking the phase B stator coils. Fig. 2 (b) shows the translator tooth shifted by a quarter of the translator tooth pitch (τt), 90 electrical degrees, where a zero net flux links the stator coils. Over the remaining 270 degrees, the pattern is repeated for the second half of the electrical cycle, but with flux flow in the opposite direction, illustrated in Fig. 2(c) and Fig. 2(d). For machines with a small pole pitch, a rapid change in the flux linkage can be achieved with a small translator displacement. The full 360 degrees of the no-load flux linkage waveform corresponds to a translator movement of one translator tooth pitch – 24 mm in this case. This conversion of low rate of change of mechanical position to a high rate of change of flux is known as magnetic gearing and is the driving force behind investigation of this machine type for low speed applications.

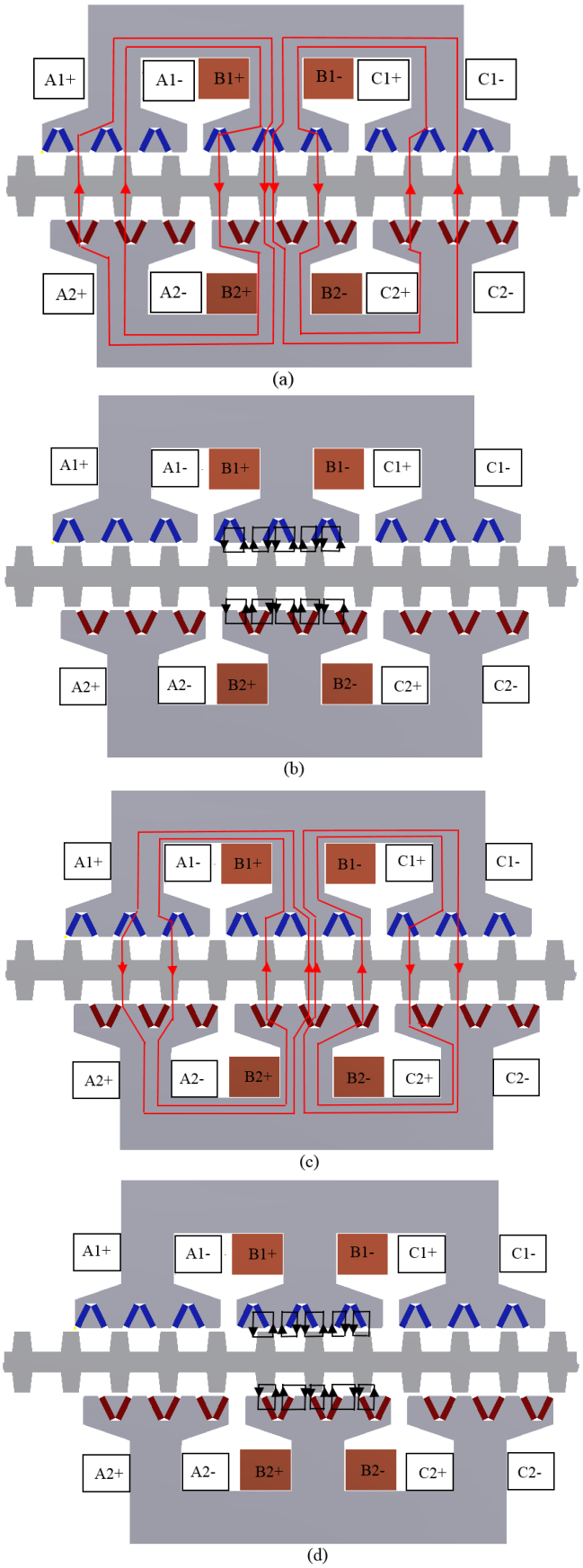

Fig. 2. Idealized flux flow from phase B magnets, to highlight operation principle at different translator positions: (a) x=0, (b) x=1/4 τ_t (c) x=1/2 τ_t and (d) x=3/4τ_t

III. MACHINE DESIGN

A. Design constraints

This section provides an overall description of the design procedures used to achieve the optimum thrust force in the two machine topologies. The design study was conducted using 2D FEA with the main parameters fixed as shown in Table I and discussed below. Current density was assumed to be 3.5 A/mm^2 RMS, and magnet mass was held constant. Although the machines are doubly salient, reluctance force in both versions is negligible and so phase advance was found to give no additional force. All studies hence assume an ideal sinusoidal current fully in the q axis and are initially aimed at maximising force compared to the surface mounted version.

B. IMCP machine

As reported in [22], a thorough design study has been carried out for the IMCP topology to maximise force for a fixed MMF and magnet mass. For example, Fig. 3 shows a tapered and straight version of the soft magnetic poles in a stator with fixed pole pitch. The ferromagnetic pole ratio F_{pr}, is defined as the ratio of the ferromagnetic pole tip to the translator tooth pitch. Fig. 4 shows the effect of varying ferromagnetic pole ratio on the thrust force. It can be seen that the highest thrust force can be achieved when F_{pr} is 0.33, which was hence selected. This is a balance between the reduction in leakage due to the introduction of tapering, and the tooth-tips starting to saturate at low F_{pr}.

C. VCP machine

In consequent pole machines, higher MMF can be produced by making the magnet pitch larger than the consequent pole pitch [23, 24]. In this study, therefore, in order to allow more room for V-shape PM arrays the magnet pole span is designed to be bigger than the consequent pole span as shown in Fig. 5. In order to determine the optimal magnet span, the magnet span ratio (m_{sr}), which is defined as the ratio of magnet span (m_s) to the stator tooth width (s_{tw}) has been investigated for a fixed magnet mass and fixed coil MMF. Results presented in [18] show that this topology has a maximum force capability at an m_{sr} ratio of 0.22. At lower values of m_{sr}, the triangle iron spacers became too small and saturate, Fig. 6(a), whereas at higher ratios, the consequent poles saturate, Fig. 6(b).

Other key geometry parameters identified in Fig. 5 have been investigated including the PM width and the PM thickness. In total, six variants of the PM dimensions, all with a fixed volume, are shown in Fig. 7 and described in Table II. They have been analysed for a maximum average thrust force and minimum cogging force. It was found that design A gave the highest average thrust force and minimum cogging force – corresponding to the longest magnet length and hence largest triangular piece. Moreover, this design can offer the optimal airgap flux density due to the flux concentration effect, which in turn can improve the power factor [8].

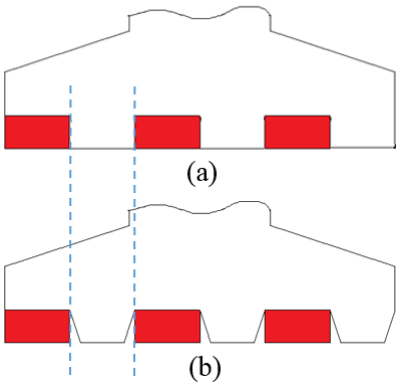

Fig. 3. The IMCP machine with (a) straight teeth and (b) tapered teeth

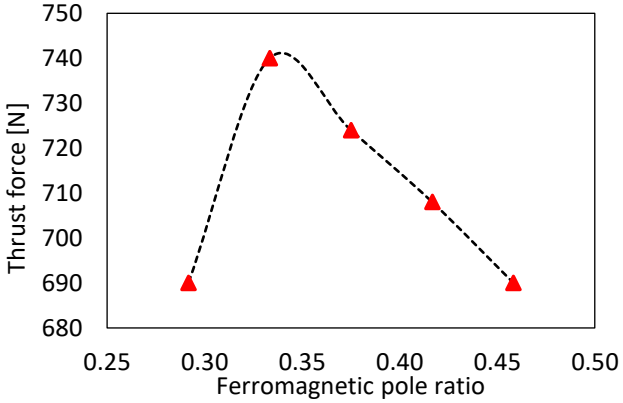

Fig. 4. Varying the taper on force performance

TABLE I
KEY PARAMETERS FOR BOTH MACHINES

Parameter	IMCP	VCP
Number of phases	3	
Translator pitch [mm]	24	
Pole pitch [mm]	12	
Airgap length [mm]	1	
Number of turns/coil	90	
Translator tooth height [mm]	10	
Machine axial length [mm]	50	
Stator tooth width [mm]	72	
Magnet remanence [T]	1.24	
Rated speed [m/s]	1.2	
Magnet width [mm]	12	
Magnet thickness [mm]	6	3
Number of the total PMs	18	36

TABLE II
PM DIMENSIONS AND V-ANGLE FOR SIX DESIGNS OF VCP

Design type	A	B	C	D	E	F
PM width [mm]	12	10	9	8	7.5	6
PM thickness [mm]	3	3.6	4	4.5	4.8	6
PM volume [cm^3]	64.8					
V-angle [degrees]	52.5	58.1	59.6	61.8	62.8	50.8

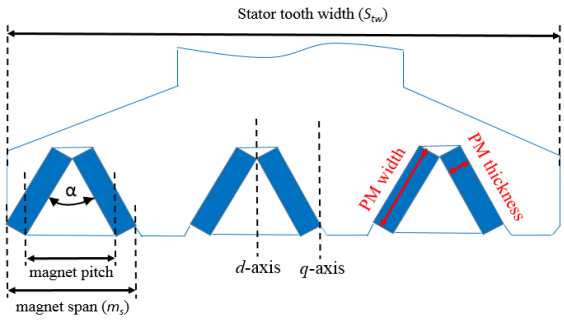

Fig. 5. Geometrical parameters

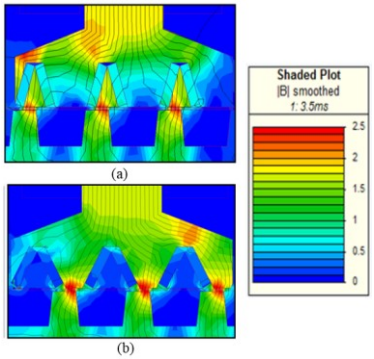

Fig. 6. Flux density at rated current and positions of maximum force for m_{sr} 0.18 and 0.24

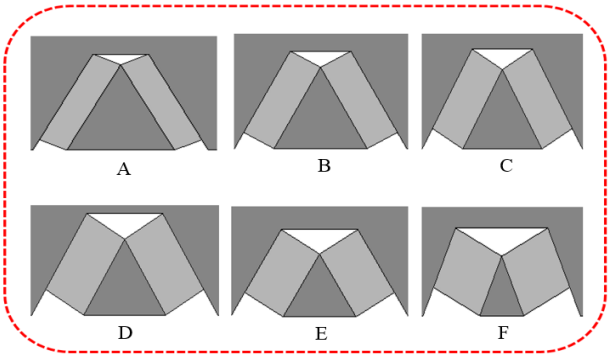

Fig. 7. Alternative designs investigated – all with a fixed PM volume

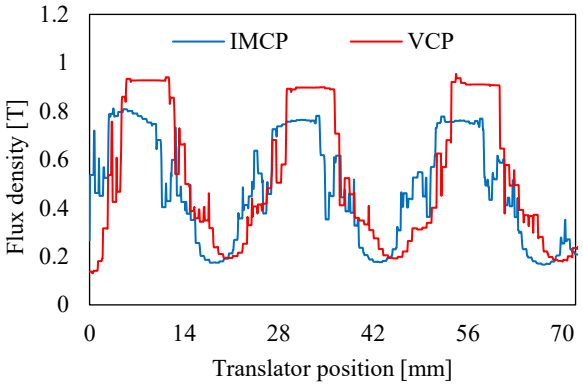

Fig. 8. Comparison of no-load airgap flux density for both designs under one stator tooth

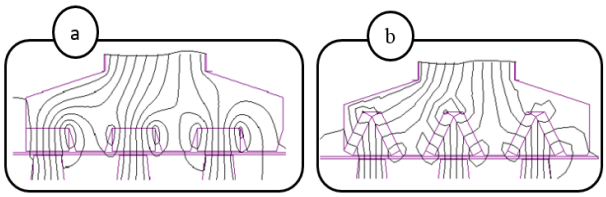

Fig. 9. No-load field distribution for IMCP and VCP machines

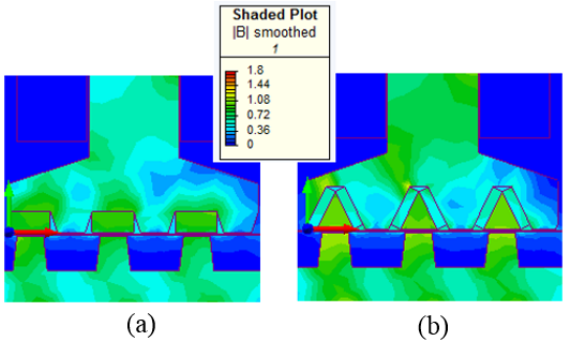

Fig. 10. No-load flux density plot for (a) IMCP machine (b) VCP machine

IV. Analysis and Comparison

2D FEA simulation results of the two designs have been used to compare these topologies. Key results are listed in Table III and discussed below.

A. No-load performance

The no-load airgap flux density and magnetic field distribution are calculated in 2D FEA in order to analyse the machine operation. Fig. 8 illustrates the radial component of the airgap flux density distributions in the upper airgap due to the PMs. The maximum airgap flux density for the IMCP and VCP machines are shown to be 0.8 T and 0.95 T respectively.

The field distribution predicted by FEA for both the consequent pole machines studied here at no-load is plotted in Fig. 9. Compared to the surface mounted magnet VPM machine, consequent poles are known to give a significant reduction of the leakage flux, leading to an increase in the main flux [2, 13, 19]. Flux concentration in the VCP machine results in a further increase in the main flux, as shown in Fig. 9, reducing the proportion of flux leakage and further still. Fig. 10 shows the no-load flux density distribution for a

TABLE III
Performance Comparison

Item	IMCP	VCP
Back EMF [V]	48	59
Iron loss [W]	17	19
Eddy current loss in PMs [W]	1.08	1.26
Copper loss [W]	62	62
Total losses [W]	80.1	82.26
Efficiency [%]	91.7	92.3
Average thrust force [N]	740	818
Force ripple [%]	7	5.8
Peak to peak cogging force [N]	62	55
Force/ PM volume [N/cm^3]	11.4	12.6
Force/ machine volume [N/m^3]	37×10^4	40.9×10^4
Shear stress [kN/m^2]	63.8	70.5
Power factor	0.5	0.65

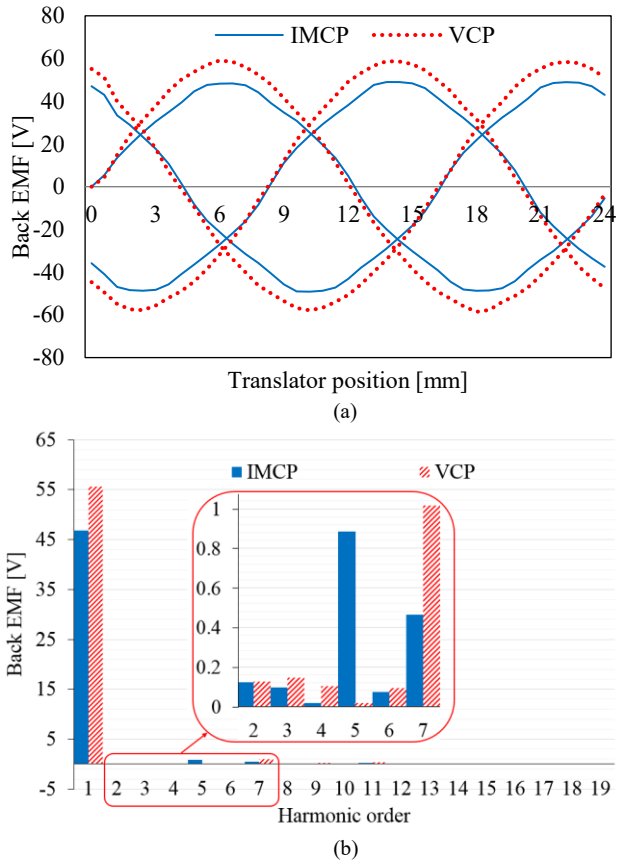

Fig.11. Comparison of (a) No-load back EMF waveforms and (b) harmonics

single stator tooth for both designs. It can be seen that the flux density of the V-shape consequent pole machine is higher than that of its counterpart.

Assuming the same rated speed, number of turns per phase, net mass and translator pitch, the higher airgap flux leads the VCP machine to have a higher no-load back EMF– as shown in Fig. 11(a). It can be seen that the peak value of the no-load back EMF of the VCP machine can achieve 59V, compared with 48V from the IMCP machine – i.e. 22.9% higher. Moreover, the waveform of the VCP machine is more sinusoidal than that of the IMCP design, shown as a

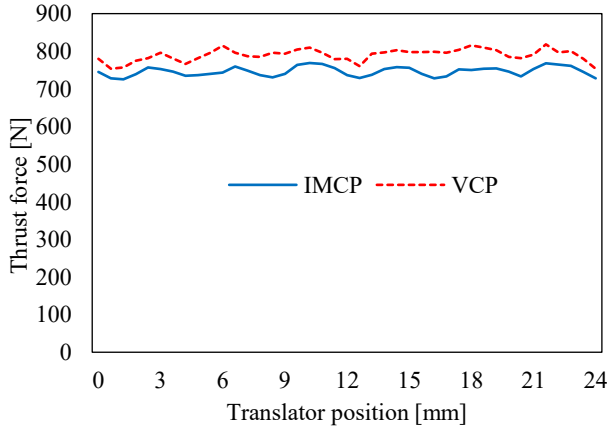

Fig.12. Thrust force waveforms for IMCP and VCP machines

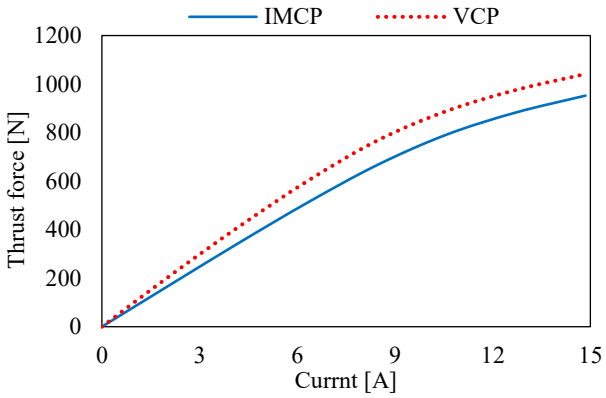

Fig.13. Thrust force capability for IMCP and VCP machines

reduction in the 5th harmonic in Fig. 11(b). EMF harmonics are heavily influenced by magnet flux leakage paths, which in the case of the VCP machine have been suppressed by elimination of the iron rib. The analogy in a conventional surface mount PM machine would be varying the space between magnets, or varying the stator tooth gap, both known methods of tuning out harmonics.

B. Force Capability

The thrust force waveforms of the IMCP and VCP machines are compared in Fig. 12 for a sinusoidal current with 3.5A/mm^2 RMS current density. The machines are assumed to be connected to an ideal converter manipulating the terminal voltage to get a sinusoidal current in phase with the no-load back EMF – i.e. in the q-axis. As shown in Table III, the VCP topology has a 10.5% higher average thrust force of 818N. The corresponding force ripple of the VCP machine is 5.8%, lower than that of the IMCP machine. This follows from the back EMF waveforms. In this publication, the force ripple is defined as ratio of the peak to peak force to the average force is which can be given by:

$$F_{ripple} = \frac{F_{max} - F_{min}}{F_{avg}} \text{x}100\% \qquad (1)$$

where F_{max}, F_{min} and F_{avg} are the maximum value, minimum value and average value of the thrust force.

By using zero *d-axis* control, the characteristics of the thrust force with respect to the applied current for both designs are compared in Fig. 13. It can be seen that in both machines as the armature current increases the thrust force is increased linearly until the applied current reaches its rated value. At higher currents, magnetic saturation in the iron core makes the increase of thrust force for both machines non-linear. The average thrust density of the machines can be calculated according to (2) and Table III confirms the VCP machine can offer a 10.5% higher force density. The shear stress, defined in (3) of the two machines at 3.5A/mm^2 is 70.5kN/m^2 and 63.8kN/m^2 respectively for the VCP and IMCP machines. By way of comparison, a value of 45 kN/m^2 was reported for an estimated current density of 3.9 A/mm^2 [25] for another VPM machine. Therefore, the VCP machine can offer competitive shear stress for a lower current density

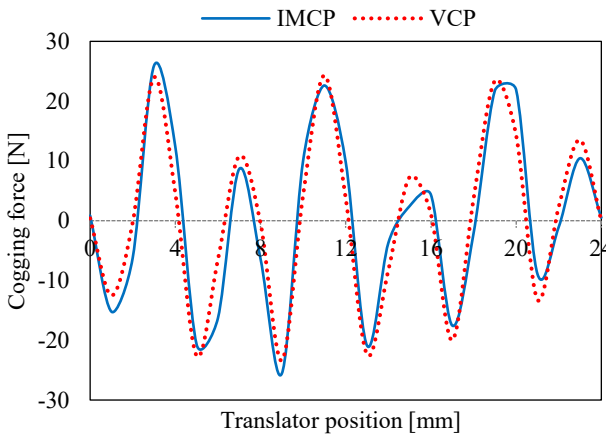

Fig.14. Cogging force waveforms for IMCP and VCP machines

than that proposed elsewhere.

$$F_d = \frac{F}{V_m} \tag{2}$$

$$\sigma = \frac{F}{A_a} \tag{3}$$

In (2) and (3) F_d is the force density, V_m is the machine volume, σ is the shear stress and A_a is the airgap area.

C. *Cogging Force*

Cogging is a common phenomenon caused by the interaction between stator PMs and translator teeth at no load and can lead to mechanical vibration and acoustic noise. In linear PM machines both slot effect and longitudinal end effects contribute to cogging force, producing larger cogging force compared to their rotary counterparts. The cogging force waveforms for both the IMCP and VCP machines are compared in Fig. 14. It can be seen that the peak to peak cogging force of the VCP machine is 11.3% lower than the IMCP machine. Once more, this is due to the improved distribution of flux in the airgap in the V shape machine [26] giving a THD of only 2%. In V-shape topology, the shape of the flux barrier is known to reduce the cogging force [26, 27] meaning that the absence of the iron ribs contributed to the cogging force reduction in the proposed VCP machine.

D. *Power factor*

For this class of machine, high inductance and corresponding low operating power factor is inherent, and for a generator this means they can only be used when connected to an over-rated converter. For VPM machines, by ignoring the resistance of the stator winding the power factor can be improved by either increasing the flux linkage or minimising the inductance as stated in [1, 8, 12, 28], which can be verified by (4).

$$PF = \frac{1}{\sqrt{1 + \left(\frac{L_s I}{\Psi_m}\right)}} \tag{4}$$

Where L_s is the synchronous inductance, I is the phase current in RMS and Ψ_m is the PM flux linkage. In general, the V-shape topologies have high inductance resulted from the low reluctance path. However, removal of the iron ribs increase the q axis reluctance path due to the increase in the q axis airgap length [27, 29], which can influence the value of the inductance. Therefore, the inductance of the VCP machine is only 2% higher than that of the IMCP machine, 16.3mH.

Assuming the converter controls the current to be sinusoidal and in phase with the back EMF, and further assuming the resultant terminal voltage is sinusoidal, the power factor is obtained by the cosine of the phase angles between them. In the FEA with the current source, the terminal voltage can be calculated by the voltage equation given in (5).

$$V_a = e + L_s \frac{di_a}{dt} + R_a i_a \tag{5}$$

The terminal voltage in the electrical machine, V_a is the sum of the voltage drop across the armature resistance, $i_a R_a$, the induced voltage of the stator winding, $L_s \cdot di_a/dt$, and the no-load back EMF, e. It was found that the phase angles between phase current and terminal voltage were 46^0 and 60^0, corresponding to a power factor of 0.65 for the VCP machine compared with 0.5 for the IMCP machine. Thus, it can be concluded that the flux concentration design not only improves PM utilization but can also be operated at a higher power factor at rated current [8]. This improvement is similar in magnitude to that achieved in [30] where a secondary DC excitation coil was used.

Fig. 15 shows the variation of the power factor with respect to the current density. It can be observed that if the real power of the two machines is matched by reducing the current density in the VCP machine by around 10%, the

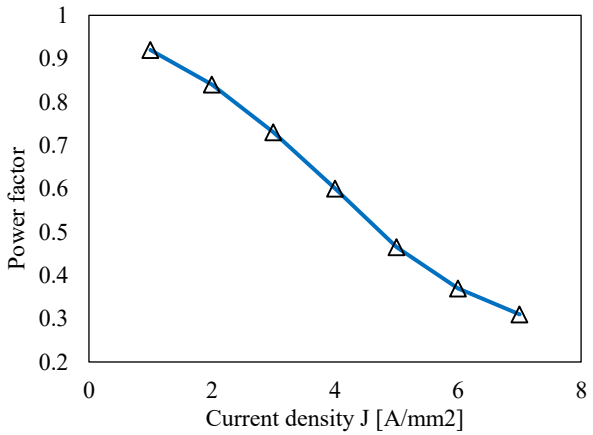

Fig.15. Variation of the power factor with respect to the current density

operating power factor increases to 0.71.

E. *Investigation of demagnetisation resistance*

In this section, the resistance of magnet demagnetisation for the VCP machine is investigated following the same method adopted in [8]. It is expected that this type of magnet arrangement has a better demagnetisation resistance compared to the surface-mounted arrangement [31]. The risk of demagnetization during the no-load three phase short-circuit fault has been evaluated. A prediction of where demagnetisation is most likely to occur in the regions of the PMs can be attained using FEA. Fig. 16 (a) shows plot taken form FEA under the three phase short-circuit current showing that there is almost no demagnetization part during this condition.

Further investigation on demagnetization capability under overloading current, i.e. 2 p.u. has been made. In this investigation it is assumed that the phase current is applied in phase with the back EMF. The demagnetization prediction under the overloading condition assuming a magnet temperature of 100 °C is shown in Fig. 16(b). As for the previous figures, the blue color represents the safe area (non-demagnetized area). Form the figure it can be observed that at 100 °C there is no risk of PM demagnetization under the overloading condition. The flux density distribution under this condition is plotted in Fig.16 (c), in which the minimum values of the flux density can be seen within the PMs are above the knee point of the B-H curve of NdFeB (N42H).

The aforementioned analysis gives an indication of that the proposed machine can remain safe at any given condition during a healthy or faulty operation.

F. *Losses and Efficiency*

The predicted losses for both machines at rated load operation were calculated and compared as shown in Table III. The copper loss is seen to dominate and as both machines operate with a fixed current density and coil area, it is equal in both machines. The VCP machine has a higher iron loss due to the increase in the airgap flux density.

The mechanical power is given by (6) and efficiency (7).

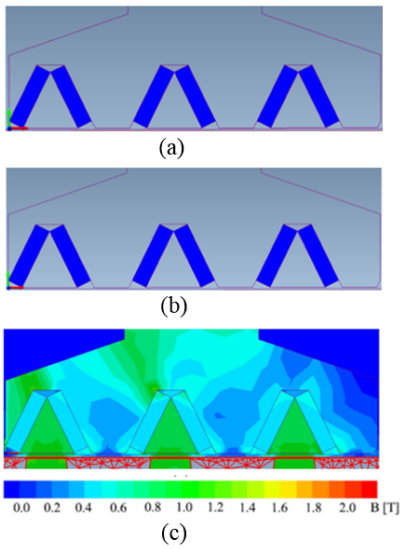

Fig.16. FEA result of demagnetisation prediction (a) short circuit current (b) overloading condition at 100 °C (c) Flux density distribution under overloading condition at 100 °C

$$P_{\text{mech}} = F \cdot v \tag{6}$$

$$\eta = \frac{P_{out}}{P_{out}+P_{cu}+P_{iron}} \tag{7}$$

where P_{out}, P_{cu}, and P_{iron} are the output power, copper loss, and iron loss, respectively. The two machines in Table III have different force capability at rated current and hence have a different power rating. Even though the VCP machine has slightly higher losses, it still achieves a marginally higher efficiency at over 92%.

V. PROTOTYPE

A. *Discussion of build*

Both topologies discussed in this paper have been built and tested in the laboratory. The stators and translator are made from lamination packs as shown in Fig. 17 (a), (b) and (c). They were tested by a linear ball screw mounted to the bed plate shown in Fig. 18. The translator has been assembled using a rigid and strong non-metallic non-magnetic material (Tufnol), which insulates the translator from being in direct contact with the aluminium support used in accommodating the bearings. Tufnol is about half the density of aluminium. The laminated translator has been sandwiched between the Tufnol bars and held together by inserting carbon fibre rods all the way through the structure via the pre-drilled holes. This allowed the authors to design a thin translator core back. Fig. 17 (c) illustrates the translator components prior to assembly.

An aluminium housing was designed to accommodate the translator through a set of linear guides and carriages allowing the stator aluminium support of both machines to be used, as shown in Fig. 17 (d).

B. *Validation of models*

During the dynamic tests, the prototypes have been directly driven by the ball screw actuator at a maximum velocity of 0.37 m/s. Fig 19(a) compares the simulated and measured no-load back EMF waveforms for the IMCP machine. It can be seen that the peak value of the measured phase no-load back EMF is 14.2V, which is 7% lower than that obtained from the transient FEA. This is potentially attributable to the end effect, construction defects or incorrect material properties, see for example [32]. The experimental results verify that the three phase waveforms are electrically shifted by 120°, the two machines are feasible to manufacture and operate as intended.

A comparison of the simulated and measured phase no-load back EMF waveforms for the VCP machine is shown in Fig. 19 (b). There is good agreement between measured and simulated results with an error of 6.5%. It can also be seen that the measured waveforms are 120 electrical degrees apart, confirming the displacement of stator teeth. By comparing the measured data for both prototypes it can be observed that

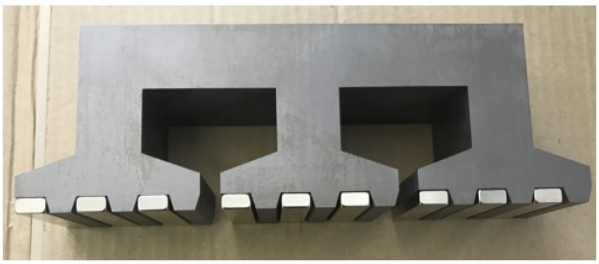

(a)

(b)

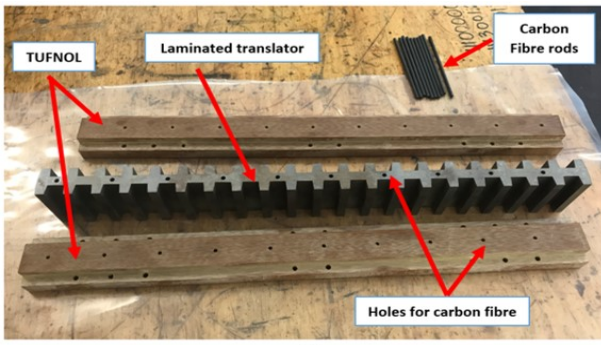

(c)

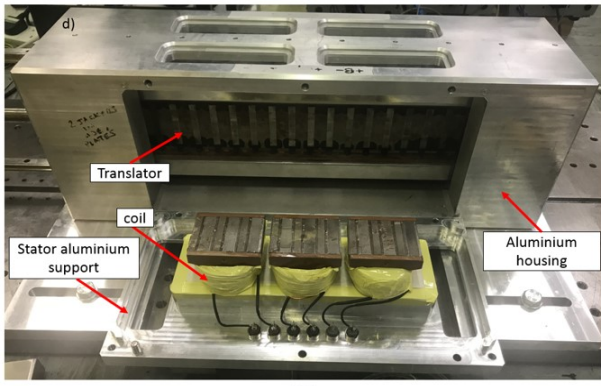

(d)

Fig.17. Prototype laminations for (a) IMCP (b) VCP (c) the translator and (d) aluminium housing and aluminium stator support

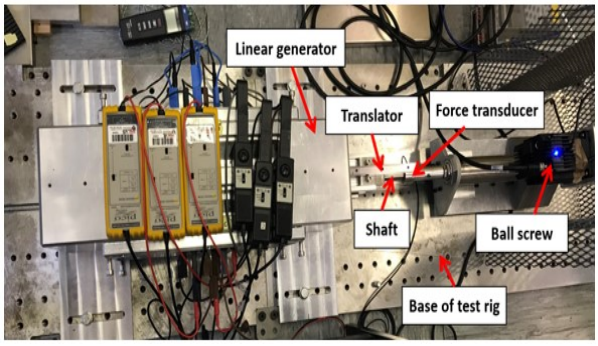

Fig.18. Test layout

the VCP machine produces a 20% higher amplitude no-load back EMF.

The cogging force has been measured statically for both prototypes using a force transducer. The measurement of the cogging force was performed without injecting current to the stator winding. The translator has been directly driven by a programmable actuator to positions with an interval of 1 mm and measurements recorded over one electrical cycle, corresponding to a displacement of 24 mm. Fig. 20 compares the experimental and FEA cogging force for both machines – measured results for both machines show an 8% and 5.9% lower peak to peak magnitude for the IMCP and VCP machines, respectively. The difference between predicted and measured force for both machines partially results from the sensitivity of the force transducer and its cable to any slight touch or movement, combined with a small error in the position due to interference caused by the electromagnetic force and a fairly coarse resolution of the load cell.

To investigate rated force of the IMCP machine, a DC current of 10 A was applied to a single phase with -5 A applied to the remaining phases. For the VCP machine, 9 A was used to give the same predicted force. The variation of the static DC force with respect to the translator position for both prototypes is plotted in Fig. 21. For both prototypes the measured static DC force is lower than the simulated values, potentially caused by the translator deviation from the desired position which might be altered under the electromagnetic force as

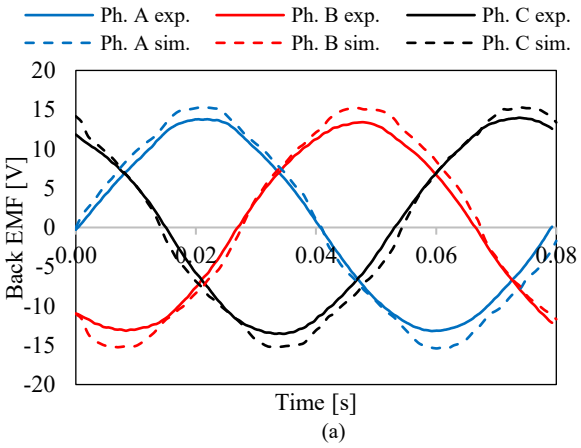

(a)

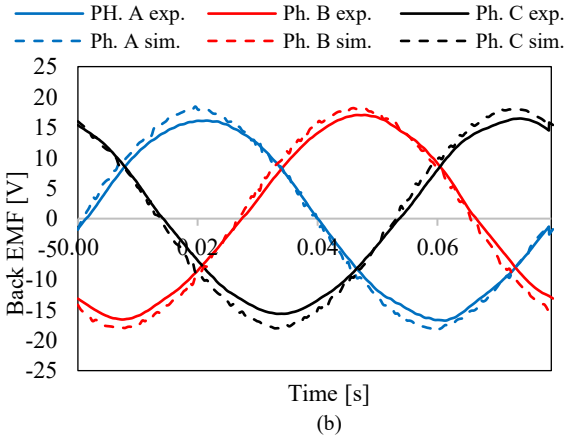

(b)

Fig.19. back EMF results (a) IMCP machine (b) VCP machine

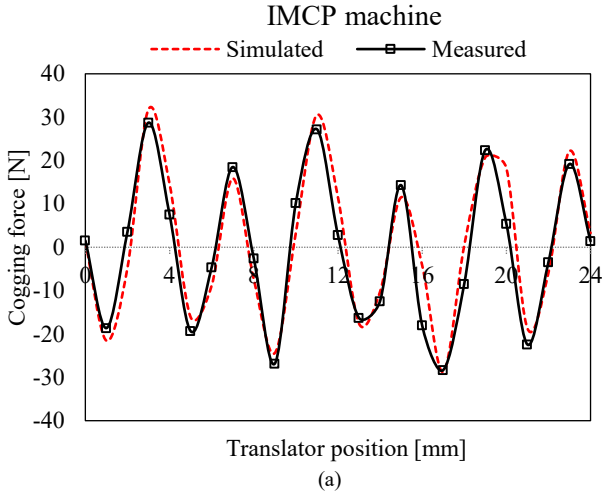

Fig.20. Cogging force waveforms (a) IMCP machine (b) VCP machine

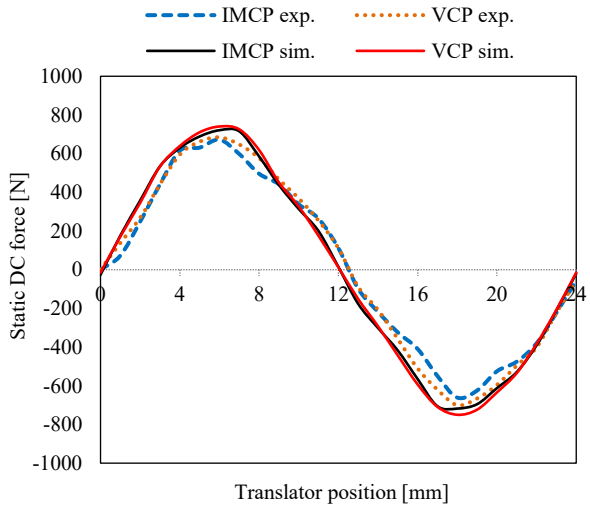

Fig.21. Comparison of simulated and measured static DC force for both machines. The IMCP a DC current of 10 A, whereas 9 A was used in the VCP

occurred in [25]. As the VCP machine requires only 90% of the excitation current to deliver the same force produced by that of the IMCP machine, the superiority of that machine is demonstrated. Furthermore, as the error between experimental and simulated results is consistent between both machines, manufacturing defects are similar and using the V-shape does not adversely affect the accuracy of assembly.

To validate the demagnetisation analysis conducted in section IV (E), the VCP prototype was overloaded with a double amplitude of its rated current (i.e. 2 p.u.). Then, the back EMF values have been measured after the overloading test and compared to that values presented in Fig. 19 (b). The results show that the peak values of the back EMF remained the same, which confirms that there is no risk of PM demagnetisation [33].

VI. CONCLUSION

Two versions of consequent pole Vernier hybrid machine have been investigated: an inset consequent pole and a V-shape flux concentrated version. Under the constraints of this study, the V-shape version is shown to be capable of a higher no-load back EMF, thrust force and power factor compared with the inset consequent pole machine. It can offer higher force density, higher efficiency and lower cogging force. Both machines were built and demonstrated in the laboratory to validate predictions. A current density of 3.5 A/mm2 gives a predicted shear stress of 64 and 71 kN/m2 operating at a power factor of 0.5 and 0.65 for the inset and V shape machines respectively.

Improved performance of the V-shape version allows the current to be reduced by 10% to match the shear stress of the inset machine. Under these conditions, the operating power factor of the V-shape machine is 0.71, which is 42% higher than the IMCP machine.

VII. REFERENCES

[1] N. Baloch, S. Khaliq, and B.-I. Kwon, "A high force density HTS tubular Vernier machine," *IEEE Transactions on Magnetics,* vol. 53, pp. 1-5, 2017.

[2] Z. S. Du and T. A. Lipo, "Torque performance comparison between a ferrite magnet vernier motor and an industrial interior permanent magnet machine," *IEEE Transactions on Industry Applications,* vol. 53, pp. 2088-2097, 2017.

[3] G. Xu, G. Liu, M. Chen, X. Du, and M. Xu, "Cost-effective vernier permanent-magnet machine with high torque performance," *IEEE Transactions on Magnetics,* vol. 53, pp. 1-4, 2017.

[4] W. Li, T. W. Ching, and K. T. Chau, "A new high-temperature superconducting vernier permanent-magnet machine for wind turbines," *IEEE Transactions on Applied Superconductivity,* vol. 27, pp. 1-5, 2017.

[5] M. Raza, W. Zhao, T. A. Lipo, and B.-i. Kwon, "Performance comparison of dual airgap and single airgap spoke-type permanent-magnet Vernier machines," *IEEE Transactions on Magnetics,* vol. 53, pp. 1-4, 2017.

[6] T. Yao, W. Zhao, F. Bian, L. Chen, and X. Zhu, "Design and Analysis of a Novel Modular-Stator Tubular Permanent-Magnet Vernier Motor," *IEEE Transactions on Applied Superconductivity,* vol. 28, pp. 1-5, 2018.

[7] C. Shi, D. Li, R. Qu, H. Zhang, Y. Gao, and Y. Huo, "A novel linear permanent magnet vernier machine with consequent-pole permanent magnets and Halbach permanent magnet arrays," *IEEE Transactions on Magnetics,* vol. 53, pp. 1-4, 2017.

[8] D. Li, R. Qu, and T. A. Lipo, "High-power-factor vernier permanent-magnet machines," *IEEE transactions on industry applications,* vol. 50, pp. 3664-3674, 2014.
[9] T. W. Ching, K. T. Chau, and W. Li, "Power factor improvement of a linear vernier permanent-magnet machine using auxiliary DC field excitation," *IEEE Transactions on Magnetics,* vol. 52, pp. 1-4, 2016.
[10] I. Boldea, *Linear electric machines, drives, and MAGLEVs handbook*: CRC press, 2013.
[11] X. Zhu, J. Ji, L. Xu, and M. Kang, "Design and Analysis of Dual-Stator PM Vernier Linear Machine With PMs Surface-Mounted on the Mover," *IEEE Transactions on Applied Superconductivity,* vol. 28, pp. 1-5, 2018.
[12] N. Baloch, S. Khaliq, and B.-I. Kwon, "HTS dual-stator spoke-type linear vernier machine for leakage flux reduction," *IEEE Transactions on Magnetics,* vol. 53, pp. 1-4, 2017.
[13] D. Li, R. Qu, J. Li, and W. Xu, "Consequent-pole toroidal-winding outer-rotor vernier permanent-magnet machines," *IEEE Transactions on Industry Applications,* vol. 51, pp. 4470-4481, 2015.
[14] Y. Gao, R. Qu, D. Li, J. Li, and G. Zhou, "Consequent-pole flux-reversal permanent-magnet machine for electric vehicle propulsion," *IEEE Transactions on Applied Superconductivity,* vol. 26, pp. 1-5, 2016.
[15] N. Baloch, B.-i. Kwon, and Y. Gao, "Low-Cost High-Torque-Density Dual-Stator Consequent-Pole Permanent Magnet Vernier Machine," *IEEE Transactions on Magnetics,* pp. 1-5, 2018.
[16] Z. Liang, Y. Gao, D. Li, and R. Qu, "Design of a novel dual flux modulation machine with consequent-pole spoke-array permanent magnets in both stator and rotor," *CES Transactions on Electrical Machines and Systems,* vol. 2, pp. 73-81, 2018.
[17] S. Yang, N. J. Baker, B. C. Mecrow, C. Hilton, G. Sooriyakumar, D. Kostic-Perovic*, et al.*, "Cost reduction of a permanent magnet in-wheel electric vehicle traction motor," in *Electrical Machines (ICEM), 2014 International Conference on*, 2014, pp. 443-449.
[18] A. A. Almoraya, N. J. Baker, K. J. Smith, and M. A. H. Raihan, "A New Configuration of a Consequent Pole Linear Vernier Hybrid Machine with V-shape Magnets," in *2018 XIII International Conference on Electrical Machines (ICEM)*, 2018, pp. 2002-2008.
[19] L. Xu, G. Liu, W. Zhao, and J. Ji, "Hybrid Excited Vernier Machines with All Excitation Sources on the Stator for Electric Vehicles," *Progress In Electromagnetics Research,* vol. 46, pp. 113-123, 2016.
[20] G. Xu, L. Jian, W. Gong, and W. Zhao, "Quantitative comparison of flux-modulated interior permanent magnet machines with distributed windings and concentrated windings," *Progress In Electromagnetics Research,* vol. 129, pp. 109-123, 2012.
[21] N. J. Baker, M. A. H. Raihan, A. A. Almoraya, J. W. Burchell, and M. A. Mueller, "Evaluating Alternative Linear Vernier Hybrid Machine Topologies for Integration Into Wave Energy Converters," *IEEE Transactions on Energy Conversion,* vol. 33, pp. 2007-2017, 2018.
[22] A. A. Almoraya, N. J. Baker, K. J. Smith, and M. A. H. Raihan, "Development of a double-sided consequent pole linear vernier hybrid permanent-magnet machine for wave energy converters," in *Electric Machines and Drives Conference (IEMDC), 2017 IEEE International*, 2017, pp. 1-7.
[23] D. Li, R. Qu, J. Li, and W. Xu, "Consequent-pole toroidal-winding outer-rotor vernier permanent-magnet machines," *IEEE Trans. Ind. Appl.,* vol. 51, pp. 4470-4481, 2015.
[24] X. Liu, C. Zou, Y. Du, and F. Xiao, "A linear consequent pole stator permanent magnet vernier machine," in *Electrical Machines and Systems (ICEMS), 2014 17th International Conference on*, 2014, pp. 1753-1756.
[25] Y. Du, M. Cheng, K. T. Chau, X. Liu, F. Xiao, W. Zhao*, et al.*, "Comparison of linear primary permanent magnet vernier machine and linear vernier hybrid machine," *IEEE Transactions on Magnetics,* vol. 50, pp. 1-4, 2014.
[26] K. Ahsanullah, R. Dutta, and M. F. Rahman, "Investigation of flat and V-shaped magnets in interior permanent magnet machine for direct drive wind turbine application," in *ECCE Asia Downunder (ECCE Asia), 2013 IEEE*, 2013, pp. 208-213.
[27] J.-H. Kim, J.-M. Seo, H.-K. Jung, and C.-Y. Won, "Analysis and Design of a Novel-Shape Permanent Magnet Synchronous Motor for Minimization of Torque Ripple and Iron Loss," *Journal of Magnetics,* vol. 19, pp. 411-417, 2014.
[28] Y. Liu, H. Y. Li, and Z. Q. Zhu, "A High-Power Factor Vernier Machine With Coil Pitch of Two Slot Pitches," *IEEE Transactions on Magnetics,* pp. 1-5, 2018.
[29] P. Liang, Y. Pei, F. Chai, and K. Zhao, "Analytical calculation of d-and q-axis inductance for interior permanent magnet motors based on winding function theory," *Energies,* vol. 9, p. 580, 2016.
[30] W. Li, T. W. Ching, and K. T. Chau, "Design and analysis of a new parallel-hybrid-excited linear vernier machine for oceanic wave power generation," *Applied Energy,* vol. 208, pp. 878-888, 2017.
[31] K.-C. Kim, K. Kim, H. J. Kim, and J. Lee, "Demagnetization analysis of permanent magnets according to rotor types of interior permanent magnet synchronous motor," *IEEE Transactions on Magnetics,* vol. 45, pp. 2799-2802, 2009.
[32] N. J. Baker, M. A. H. Raihan, and A. Almoraya, "A Cylindrical Linear Permanent Magnet Vernier Hybrid Machine for Wave Energy," *IEEE Transactions on Energy Conversion,* 2018.
[33] Y. Zhang, S. McLoone, W. Cao, F. Qiu, and C. Gerada, "Power loss and thermal analysis of a MW high-speed permanent magnet synchronous machine," *IEEE Transactions on Energy Conversion,* vol. 32, pp. 1468-1478, 2017.

VIII. BIOGRAPHIES

Ahmed A. Almoraya received his BSc degree in Electrical Engineering from Riyadh College of Technology, Saudi Arabia in 2009, and his MSc degree in Electrical Power from Newcastle University, Newcastle upon Tyne, UK in 2013. He is currently working towards his PhD degree in Newcastle University, Newcastle upon Tyne, UK. His research interests include electrical machines design for automotive and renewable energy applications.

His employment experience included the ministry of water and Technical and Vocational Training Corporation, Saudi Arabia.

Nick J. Baker received a MEng Degree in Mechanical Engineering from Birmingham University, UK, in 1999 and a Ph.D. from Durham University U.K in 2003 for work in electrical machine design for marine renewable energy devices. He is presently a Senior Lecturer within Newcastle University's Electrical Power Group. Nick is a machine designer with research projects across the automotive, aerospace and renewable energy sector.

Kristopher J. Smith completed an apprenticeship with British Telecom before attended Northumbria University. Here he received a BSc(Hons) in Communications & Electronic Engineering and a MSc in Microelectronic Engineering. In 2006 he joined Newcastle University to complete an Engineering Doctorate (EngD) with sponsorship from Dyson. His research focused on Power Supply Quality in Brushless Drives. After completing the doctorate Kris has moved into a Teaching Fellowship at Newcastle University. His research interests are mainly in permanent magnet machine design.

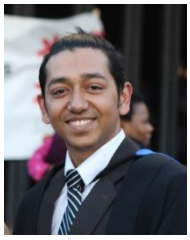

Mohammad A.H. Raihan received his B.Sc. degree in electrical engineering from the Military Institute of Science & Technology (MIST), Dhaka, Bangladesh in 2013, and his M.Sc. degree in Electrical Power Engineering from Newcastle University, Newcastle upon Tyne, U.K., in 2015. He is currently working towards his Ph.D. at Newcastle University, Newcastle upon Tyne, U.K. His research interests and experience include different rotary and linear electrical machine design for automotive applications and renewable energy generation.